

DOI: 10.54503/0571-7132-2022.65.3-315

## MULTIWAVELENGTH MONITORING OF BLAZARS PKS 2155-304 AND S5 0716+71

D.ISRAYELIAN

Received 1 June 2022

Accepted 8 August 2022

The study of multiwavelength emission properties of blazar jets has the potential to shed light on the particle acceleration and emission mechanisms taking place in them. The emission of PKS 2155-304 ( $z=0.116$ ) and S5 0716+71 ( $z=0.31$ ) bright blazars in the optical/UV, X-ray and  $\gamma$ -ray bands is investigated by analyzing data from Fermi-LAT, Swift XRT and Swift UVOT telescopes. The multiwavelength light curves of both sources in these bands show multiple peaks when the flux increased substantially. In the optical/UV bands, the flux of both sources increased above  $2 \cdot 10^{-10}$  erg cm<sup>-2</sup> s<sup>-1</sup>. The X-ray emission from PKS 2155-304 was characterized by a harder-when-brighter trend, whereas the  $\gamma$ -ray emission from S5 0716+71 showed a moderated trend of softer-when-brighter. The correlation analysis shows a strong correlation between the UV and  $\gamma$ -ray emission of PKS 2155-304, while there is a correlation between the optical/UV and X-ray emission of S5 0716+71. The observed broadband spectral energy distribution of both sources as well as the observed variability and correlations can be accounted for within one-zone synchrotron/synchrotron-self-Compton models.

Keywords: *PKS 2155-304; S5 0716+71;  $\gamma$ -rays; X-rays; blazars*

1. *Introduction.* Blazars, a special type of active galactic nuclei whose jet makes a small viewing angle to the observer, are among the most powerful long-lived objects. Blazars are the dominant population of extragalactic sources in the  $\gamma$ -ray sky. Blazars are usually sub-divided into flat-spectrum radio quasars (FSRQs) and BL Lac objects. The latter have weak or absent emission lines while FSRQs are characterized with strong emission lines (equivalent width,  $EW > 5\text{\AA}$ ) in their spectra. BL Lac objects are further classified into three subtypes based on the peak frequency of synchrotron emission: high synchrotron peaked BL Lacs (HBL when  $\nu_s > 10^{15}$  Hz), intermediate synchrotron peaked BL Lacs (IBL when  $10^{14} \text{ Hz} < \nu_s < 10^{15} \text{ Hz}$ ), or low synchrotron peaked BL Lacs (LBL when  $\nu_s < 10^{14} \text{ Hz}$ ) [1,2].

The spectral energy distribution (SED) of blazars is dominated by the nonthermal emission and consist of two broad components: the first (low-energy component) peaking from far infrared frequencies to X-ray energies and the second (high energy component) peaking at MeV/GeV bands. The emission in the low-energy band is highly polarized [3,4] and this component is believed to be synchrotron radiation from relativistic electrons in the jet. The origin of the second component is still under debate. Most likely, this component is due to inverse

Compton scattering of synchrotron and/or external photons [5,6]. The nature of the external photons depends on the location of the emission region; these can be photons either from the disk or those reprocessed from the broad-line region or those from the infrared torus. However, the hadronic origin of this component, when the emission is due to the interaction of protons, cannot be excluded. This component can be also produced from the interaction of relativistic protons either from their synchrotron emission [7] or from the secondary particles from pion decay [7-11]. In the latter case, the jets of blazars are also sources of very high energy (VHE;  $>100$  GeV) neutrinos [12-21].

The emission from blazar jets ranges across all accessible bands in the electromagnetic spectrum so their multi-wavelength observations are essential for the study of the origin of their emission. Also, the emission from blazars shows variability in all the bands, from radio to VHE  $\gamma$ -ray bands, on timescales ranging from years to only a few minutes. Sometimes (but not always) there is a correlated variability between two bands which indicates that the same process might be responsible for the emission in these bands. Now, the accumulated amount of data permits a detailed variability study in almost all the bands which is crucial for understanding the complex physics of blazars. For example, the MAGIC observation of BL Lac blazar on 15 June 2015 showed a flare with a maximum flux of  $(1.5 \pm 0.3) \cdot 10^{-10}$  photon  $\text{cm}^{-2} \text{s}^{-1}$  and a halving time as short as  $26 \pm 8$  min [22]. Or in the high energy (HE  $> 100$  MeV) band, the Fermi Large Area Telescope (Fermi-LAT) observations of 3C 279 on 16 June 2015 showed an high-amplitude variability (the  $\gamma$ -ray flux was as high as  $\sim 3.6 \cdot 10^{-5}$  photon  $\text{cm}^{-2} \text{s}^{-1}$ ) when the source flux variability was resolved down to 2-minute binned timescales, with flux doubling times of less than 5 minutes [23]. Similarly, the long-term variability has been extensively investigated also in the radio-optical bands where the data collected over decades are available [24,25].

The multiwavelength variability study of blazars has recently entered a new era. There is a large amount of  $\gamma$ -ray data available from continuous observations of blazars in the HE band by Fermi-LAT. Also Neil Gehrels Swift Observatory [26], (hereafter Swift) performed a large number of observations of single objects. The Swift satellite with three instruments on board - the UV and Optical Telescope (UVOT) [27], the X-Ray Telescope (XRT) [28] sensitive to the 0.3-10.0 keV band, and the Burst Alert Telescope (BAT) [29] sensitive to the 15-150 keV band - is an ideal instrument for simultaneous observation of blazars in the X-ray, Optical, and UV bands. The combination of the data from Swift observations with data from Fermi-LAT in the  $\gamma$ -ray band, will provide a unique possibility to investigate both emission components in the broadband SED of the blazars.

Variability studies in each band are crucial to identify the timescale of flux variability which in its turns allows to constrain the size and location of the

emitting region. At the same time, intra-band variability studies allow to identify correlated or anti-correlated variabilities in different bands which can shed light on the physical processes responsible for multiwavelength emission from blazars. Considering the large number of blazars observed more than 100 times by Swift (see Fig.1 in Giommi, et al. 2021) [30], a tool that automatically downloads and analyzes data from Swift UVOT observations of blazars was developed. This allows to process a large amount of optical/UV data accumulated after the launch of Swift satellite. As an application of the tool, the data from observations of two well-known blazars, PKS 2155-304 and S5 0716+71, was reduced. Also, the X-ray and  $\gamma$ -ray data were analyzed and compared with optical/UV data allowing to investigate variability in different bands and investigate the origin of broad band emission from these sources.

The paper is structured as follows: the optical/UV observations of the sources is presented in Section 2. The X-ray and  $\gamma$ -ray data extraction and analysis are presented in Sections 3 and 4, respectively. The results and interpretations are given in Section 5 and the summary is presented in Section 6.

*2. Monitoring of the sources in optical/UV bands.* The Swift satellite launched in 2004 is primarily designed for observations of  $\gamma$ -ray bursts. With the three instruments on board (UVOT, XRT and BAT) and a wide energy coverage, Swift is suitable for blazar research. The range observed by Swift defines either the low-energy component or the transition region between the two components or the rising part of the inverse Compton component (depending on the type of blazar), so that these data are particularly important for theoretical modeling.

The Swift UVOT telescope can produce images in each of six filters, namely in V (500-600 nm), B (380-500 nm), U (300-400 nm), W1 (220-400 nm), M2 (200-280 nm) and W2 (180-260 nm). In order to process UVOT data from any blazar observation, a special tool was developed. Providing the name and the coordinates of the source under interest, it accesses the Swift archive, downloads all the existing observations and processes them with the standard procedure. After cleaning and filtering the data, all single observations are reduced by selecting source counts from a circular region of 5" around the source, while selecting the background counts from a 20" region away from the source. Then with the help of *uvotsource* tool it derives the magnitudes which are converted to fluxes using the conversion factors provided by Poole et al. [31] and then corrected for extinction, using the reddening coefficient  $E(B - V)$  from the Infrared Science Archive<sup>1</sup>. The tool produces the flux measured in each filter in each period for the light curve computation as well as the flux for each frequency for SED

---

<sup>1</sup> <http://irsa.ipac.caltech.edu/applications/DUST/>

calculations. The tool was extensively tested by analyzing the data from different blazar observations and comparing with the published results.

The developed tool was used to analyze all the Swift UVOT observations of PKS 2155-304 and S5 0716+71. Between 2004-2022, PKS 2155-304 were observed 300 times and S5 0716+71 - 352 times. The light curve of PKS 2155-304 is shown in Fig.1d and 1e, separating the flux in V, B, U and W1, M2 and W2 filters. It shows that during the initial observations (e.g., until MJD

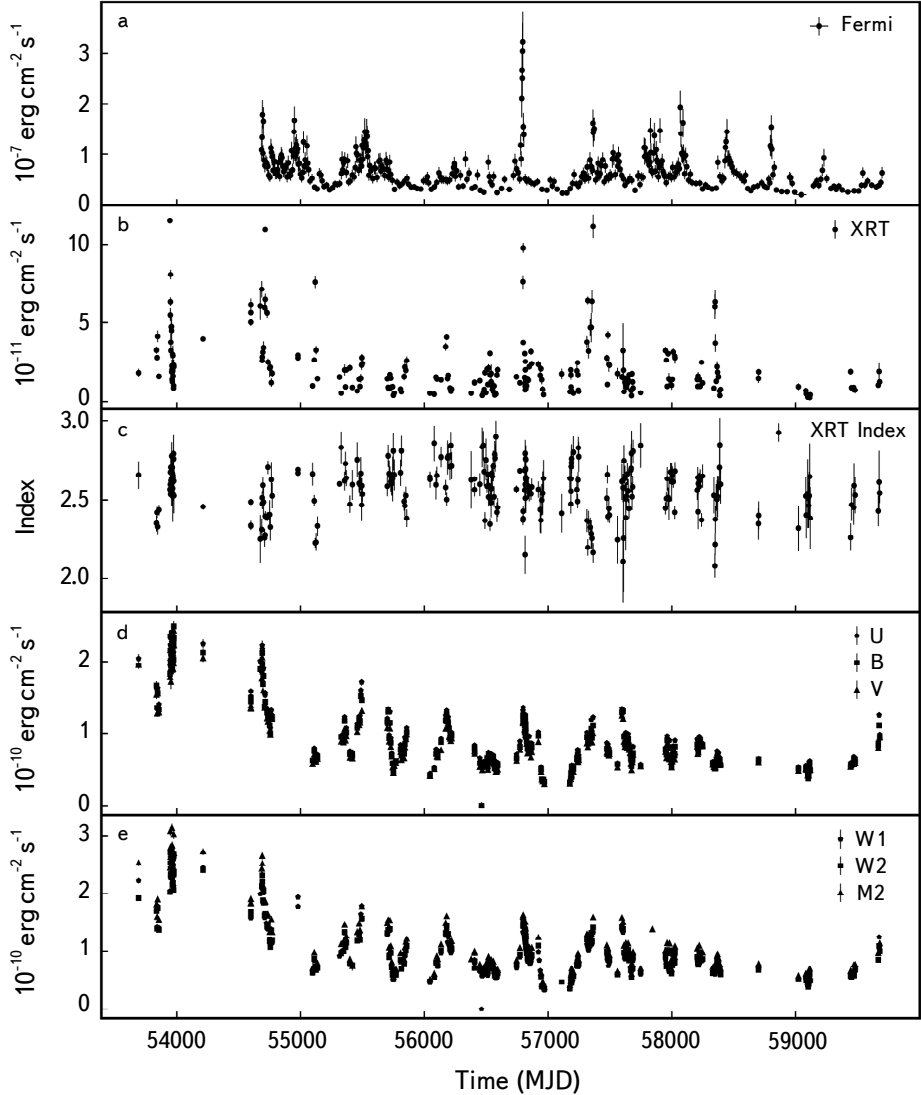


Fig.1. Multiwavelength light curve of PKS 2155-304. a) Adaptively binned  $\gamma$ -ray light curve above MeV. b) X-ray flux estimated in 2.0-10 keV band. c) X-ray photon index. d) Flux in U, B and V bands. e) Flux in W1, W2, and M2 bands.

55000) the source was in an evaluated emission state in all the considered bands. For example, in this period the highest flux of the source was  $(3.12 \pm 0.07) \cdot 10^{-10}$   $\text{erg cm}^{-2} \text{s}^{-1}$  observed on MJD 53960.85 in filter M2. Then the averaged level of source emission in optical/UV bands decreases, but a few times flux variations in all the considered filters are still evident. For example, the flux in M2 band on MJD 56046.13 was  $(5.1 \pm 0.11) \cdot 10^{-11}$   $\text{erg cm}^{-2} \text{s}^{-1}$  which increased to  $(1.60 \pm 0.03) \cdot 10^{-10}$   $\text{erg cm}^{-2} \text{s}^{-1}$  on MJD 56180.67. Such changes in consecutive

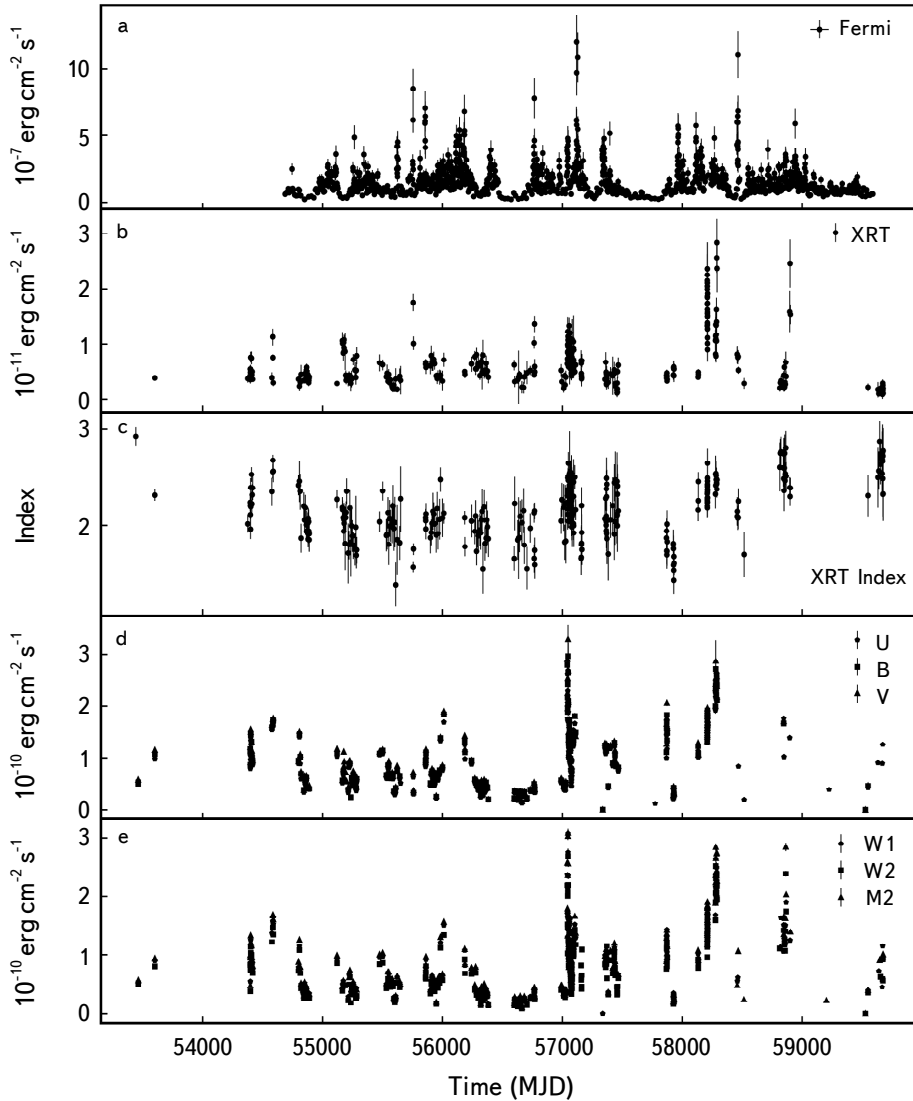


Fig.2. The multiwavelength light curve of S5 0716+71 between 04/08/2008-04/05/2022. From top to bottom: adaptively binned  $\gamma$ -ray light curve ( $>202.65$  MeV), 2.0-10 keV X-ray flux, 0.3-10 keV X-ray photon index, flux in V, B, and U filters and in W1, M2 and W2 filters.

UVOT observations can be identified during all the considered periods, which show that this source has a strongly variable optical/UV emission.

In Fig.2d and 2e, S5 0716+71 light curve in V, B, U and W1, M2 and W2 filters is shown. Two large flaring activities in optical and UV bands are evident. The first active period was observed between MJD 57030-57060 when the flux in almost all filters increased from  $\sim 5 \cdot 10^{-11} \text{ erg cm}^{-2} \text{ s}^{-1}$  to above  $\sim 2 \cdot 10^{-10} \text{ erg cm}^{-2} \text{ s}^{-1}$ . In this period, the highest flux of  $(3.28 \pm 0.09) \cdot 10^{-10} \text{ erg cm}^{-2} \text{ s}^{-1}$  was observed in filter V on MJD 57047.31. The next major flaring activity was observed between MJD 58200-58300 when the flux again increased to above  $\sim 2 \cdot 10^{-10} \text{ erg cm}^{-2} \text{ s}^{-1}$ . This source is characterized by variable optical/UV emission, i.e., the flux changes in different Swift observations. Only between MJD 56600-56800 the source was in a relatively quiescent state in the optical/UV bands: during this period, in 14 Swift observations the flux was relatively constant with a value of  $\sim 2 \cdot 10^{-11} \text{ erg cm}^{-2} \text{ s}^{-1}$ .

3. *X-ray observations of PKS 2155-304 and S5 0716+71.* Simultaneously with the optical/UV observations, the sources were observed also in the X-ray band with the Swift XRT instrument. For both sources all the data were downloaded from SSDC archive (<https://www.ssd.csi.it>) and processed using *Swift\_xrtproc* automatic tool for XRT data analysis [30]. The raw data (Level1) were downloaded, reduced, calibrated and cleaned via the XRTPIPELINE script by applying the standard filtering criteria and the latest calibration files of CALDB. The counts were extracted from a circular region of a radius of  $\sim 20$  pixels ( $47''$ ) centered on the source's position, while the background counts are taken from an annular ring centered at the sources. The tool automatically applies also pile-up correction when the sources' count rate was above  $0.5 \text{ counts s}^{-1}$ . Then it loads the ungrouped data in XSPEC (version 12.11) for spectral fitting using Cash statistics [32], modeling the source spectrum as a power-law and a log-parabola model taking the Galactic absorption column density from  $N_H$  HEASARC tool (<https://heasarc.gsfc.nasa.gov/cgi-bin/Tools/w3nh/w3nh.pl>) [33-35].

The X-ray flux and photon index variation of PKS 2155-304 are shown in Fig.1b and 1c. In the X-ray band, there are several observations when the flux in the 2.0-10 keV band substantially increased. In the low (average) state the flux is around  $(0.2-1.0) \cdot 10^{-11} \text{ erg cm}^{-2} \text{ s}^{-1}$  while in the flaring state it increases to  $> 10^{-10} \text{ erg cm}^{-2} \text{ s}^{-1}$  (e.g., in observations on MJD 53945.04, 54714.16, 57363.93). The X-ray photon index varies in time as well, on average the source is characterized with a soft photon index ( $\Gamma_X \approx 2.5$ ) but from time to time it hardens ( $\Gamma_X < 2.5$ ). It is interesting to note that around the flares on MJD 57363.93 and MJD 58350.03 when the X-ray flux increased correspondingly to  $(1.11 \pm 0.07) \cdot 10^{-10} \text{ erg cm}^{-2} \text{ s}^{-1}$  and  $(6.32 \pm 0.74) \cdot 10^{-11} \text{ erg cm}^{-2} \text{ s}^{-1}$ , the X-ray photon index was  $\Gamma_X = 2.16 \pm 0.06$  and  $\Gamma_X = 2.21 \pm 0.07$ , respectively. This is unusual for

PKS 2155-304 and it most likely corresponds to the transition region between the synchrotron and inverse Compton components.

In the X-ray band, S5 0716+71 shows several flaring periods as well. There can be identified at least three large flaring activities in Fig.2b: the first two between MJD 58140-58460 and the third one around MJD 58900 (in several other periods the X-ray flux increases as well but with smaller amplitudes). The highest flux of the source ( $2.84 \pm 0.45$ )  $\cdot 10^{-11}$  erg cm $^{-2}$  s $^{-1}$ ) was observed on MJD 58288.68 which 11.36 times exceeds the X-ray flux in the average/low state ( $\sim 2.5 \cdot 10^{-12}$  erg cm $^{-2}$  s $^{-1}$ ). The photon index variation is evident from Fig.2d, it varies around  $\Gamma_X = 2.0$ , sometimes showing harder spectra ( $\Gamma_X < 2.0$ ) but sometimes also soft spectra were observed ( $\Gamma_X > 2.2$ ). The softest index of  $\Gamma_X = 2.86 \pm 0.2$  was observed on MJD 59646.43 while the hardest one was  $\Gamma_X = 0.96 \pm 0.66$  observed on MJD 55608.93.

4.  *$\gamma$ -ray observations and data analysis.* Fermi-LAT on board the Fermi Gamma-ray Space Telescope is a pair-conversion telescope sensitive to  $\gamma$ -rays in the energy band from 20 MeV to 500 GeV. By default, being in the scanning mode, it observes the entire sky every  $\sim 3$  hours, providing a continuous view of the  $\gamma$ -ray emission from Galactic and extragalactic sources. The details on the Fermi-LAT instrument are given in Atwood et al. 2009 [36].

In this paper, the Fermi-LAT data accumulated during 2008-2022 (MET 239557417-673371821) from the observations of PKS 2155-304 and S5 0716+71 are considered. The data were processed with the standard Fermi ScienceTools version 1.2.1. The Pass 8 (P8R3) Fermi-LAT events with a higher probability of being photons (*evclass* = 128, *evtype* = 3) were analyzed using the *P8R3\_SOURCE\_V3* instrument response function. The events in the energy range from 100 MeV to 500 GeV were downloaded from a  $12^\circ$  region centered on the  $\gamma$ -ray position of PKS 2155-304 (RA = 329.71 and Dec = -30.22) and S5 0716+71 (RA = 110.49 and Dec = 71.34). With *gtselect* tool A zenith angle cut smaller than  $90^\circ$  is applied to reduce contamination by photons from Earth's atmosphere while the good time intervals are selected with *gtmktime* tool using the filter expression (*DATAQUAL* > 0) and (*LAT CONFIG* = 1). With *gtbin* tool the photons are binned into  $16^\circ.9 \times 16^\circ.9$  square region into pixels of  $0^\circ.1 \times 0^\circ.1$  and into 37 equal logarithmically spaced energy bins. Then, with the help of *gtlike* tool, a standard binned maximum likelihood analysis is performed. The fitting model includes diffuse and isotropic backgrounds, which were modeled with standard *gll\_iem\_v07* and *iso\_P8R3\_SOURCE\_V3\_v1* models and  $\gamma$ -ray sources within the region of interest. The model was created using the Fermi-LAT fourth source catalog Data Release 3 (4FGL-DR3) [37] where all sources within  $17^\circ$  around the target are included. The spectral parameters of the background sources

which are between  $12^\circ$  and  $12^\circ + 5^\circ$  were fixed to their catalog values, while the normalization and spectral parameters of the other sources were left free.

After optimizing the free parameters in the model, the source variability is investigated by estimating the flux (light curve) in shorter intervals by applying unbinned likelihood analysis. The light curve was calculated with the help of an adaptive binning method. When calculating the light curve with fixed time bins (e.g., a day or several days), the long bins will smooth out the fast variation, whereas the short bins might instead result in many upper limits, preventing the variability studies. In the adaptive binning method, the bin width is adjusted by requiring a constant relative flux uncertainty, which produces longer time intervals during lower flux levels and narrower bins when the source is in a high state. This method has been proven to be very efficient in identifying flaring activities [38-43].

The light curve of PKS 2155-304 computed above the optimal energy of 274.38 MeV is shown in Fig.1a. It shows that in several occasions the source flux increased several times (3-5 times), but the major  $\gamma$ -ray flare was observed between MJD 56770-56800 when within 37 days the flux increased from  $(5.08 \pm 0.9) \cdot 10^{-8}$  photon  $\text{cm}^{-2} \text{s}^{-1}$  to  $(3.24 \pm 0.59) \cdot 10^{-7}$  photon  $\text{cm}^{-2} \text{s}^{-1}$ . The highest flux of  $(3.24 \pm 0.59) \cdot 10^{-7}$  photon  $\text{cm}^{-2} \text{s}^{-1}$  above 274.38 MeV was observed on MJD 56795 within 15.86 minutes which is the highest  $\gamma$ -ray flux of PKS 2155-304 since the launch of Fermi-LAT. It is interesting that during this flaring event also the photon index hardened, namely when the high fluxes of  $(3.24 \pm 0.59) \cdot 10^{-7}$  photon  $\text{cm}^{-2} \text{s}^{-1}$  and  $(3.04 \pm 0.56) \cdot 10^{-7}$  photon  $\text{cm}^{-2} \text{s}^{-1}$  were observed on MJD 56795 and 56794, respectively, the  $\gamma$ -ray photon index was  $1.64 \pm 0.12$  and  $1.53 \pm 0.11$ , respectively. It shows that during this flare the  $\gamma$ -ray spectrum hardens, shifting the peak to higher energies.

A similar adaptive light curve of S5 0716+71 computed above 202.65 MeV is shown in Fig.2a. As compared with PKS 2155-304, this source shows several prolonged  $\gamma$ -ray flaring periods. The  $\gamma$ -ray flux of sources in the low states (e.g., between MJD 57570-57840) is around  $\sim 3 \cdot 10^{-8}$  photon  $\text{cm}^{-2} \text{s}^{-1}$ . The maximum  $\gamma$ -ray flux of  $(2.0 \pm 0.2) \cdot 10^{-6}$  photon  $\text{cm}^{-2} \text{s}^{-1}$  was observed on MJD 57118.61 which exceeds the flux at low states by nearly 66 times. The mean photon index in the  $\gamma$ -ray band is  $\Gamma_{mean} = 2.05$  which corresponds to a flat spectrum in  $\nu F \nu$  representation, but a hard index of  $\Gamma_\gamma = 1.59 \pm 0.10$  was occasionally observed on MJD 56079 and a soft index of  $\Gamma_\gamma = 2.63 \pm 0.23$  was observed on MJD 59356.1. In total, during nearly fourteen years of observations of S5 0716+71, there are 16 periods when the  $\gamma$ -ray photon index was  $\Gamma_\gamma < 1.7$ .

*5. Results and interpretation.* The multiwavelength data collected from blazar observations is the key to the understanding of the origin of the complex

processes taking place in relativistic jets. In this paper, the multiwavelength emission from two blazars, PKS 2155-304 and S5 0716+71, was comprehensively investigated by analyzing the Swift UVOT, Swift XRT and Fermi-LAT data accumulated in the past fourteen years. PKS 2155-304 at a redshift of  $z=0.116$  is one of the brightest HBL type objects in the Southern Hemisphere. It is an object very luminous in the UV to VHE  $\gamma$ -ray bands and has an almost featureless continuum from radio to X-ray energies as in most of the other BL Lac objects. Its multiwavelength emission observed for already more than 40 years is strongly variable in almost all bands. In radio bands, this source was discovered as part of the Parkes survey [44] and was discovered as an X-ray source by the HEAO 1 X-ray satellite [45]. In the  $\gamma$ -ray band, the source was initially observed by EGRET [46] and it was one of the first blazars observed in the VHE  $\gamma$ -ray band [47]. S5 0716+71 with a redshift of  $z=0.31 \pm 0.08$  [48] is another well-studied BL Lac bright in all bands. It shows extreme variability (e.g., in the X-ray band) and a prominent jet component, and it is a strong  $\gamma$ -ray source. The long-term monitoring of S5 0716+71 in the radio and optical bands reveals the presence of quasi-periods. The optical data accumulated during 1994-2001 indicated a period of about 3.3 years. Instead, the radio data at frequencies from 4.8 to 36.8 GHz indicate the presence of a period of 8 years [49]. The MAGIC observations in the VHE  $\gamma$ -ray band show that this source underwent an impressive outburst in January 2015 (Phase A), followed by minor activity in February (Phase B) [50]. During this flaring period the source flux increased from  $(4.1 \pm 1.1) \cdot 10^{-11} \text{ cm}^{-2} \text{ s}^{-1}$  to  $(8.9 \pm 1.1) \cdot 10^{-11} \text{ cm}^{-2} \text{ s}^{-1}$  above 150 GeV.

*5.1. Photon index versus flux variation.* The data available in the X-ray and  $\gamma$ -ray bands allows to investigate the variation of the flux as compared with the photon index. The spectral evolution observed in the photon-index-flux plane contains important information about the dynamics of the source and provides an insight into the processes responsible for the particle acceleration and cooling. As it has been shown in Kirk et al. [51], depending on the relation between the variability, acceleration and cooling timescales, a harder-when-brighter or softer-when-brighter trend will be observed in the photon index versus the flux plane. The  $\gamma$ -ray photon index of PKS 2155-304 versus the photon index is shown in Fig.3a, b, considering the entire period of Fermi-LAT observations and selecting only the period around the large flare (between MJD 56720-56850). When the entire observational period is considered with diverse properties (Fig.3b), it is hard to see any trend. In fact, applying linear-Pearson correlation test yields  $r_p = 0.02$  and  $p = 0.71$ . Similar values estimated for the flaring period yields  $r_p = 0.35$  and  $p = 0.36$ . This shows that there is no correlation between the flux and photon index, i.e., the flux and photon index are independent. On the

contrary, when considering all Swift XRT observations (Fig.3c), there is a clear indication of the harder when brighter trend. The linear-Pearson correlation test results in  $r_p = -0.55$  and  $p \ll 10^{-5}$  which shows a negative correlation between the flux and photon index, i.e., as the flux increases, the photon index decreases (hardens). Such a relation between the flux and photon index is expected when the accelerated HE electrons are cooling down, Kirk et al. [51]. When considering only the flaring period (Fig.3d), although there is a hint of a harder-when-brighter trend, the data are not enough for a statistically significant claim ( $r_p = -0.28$  and  $p = 0.12$ ).

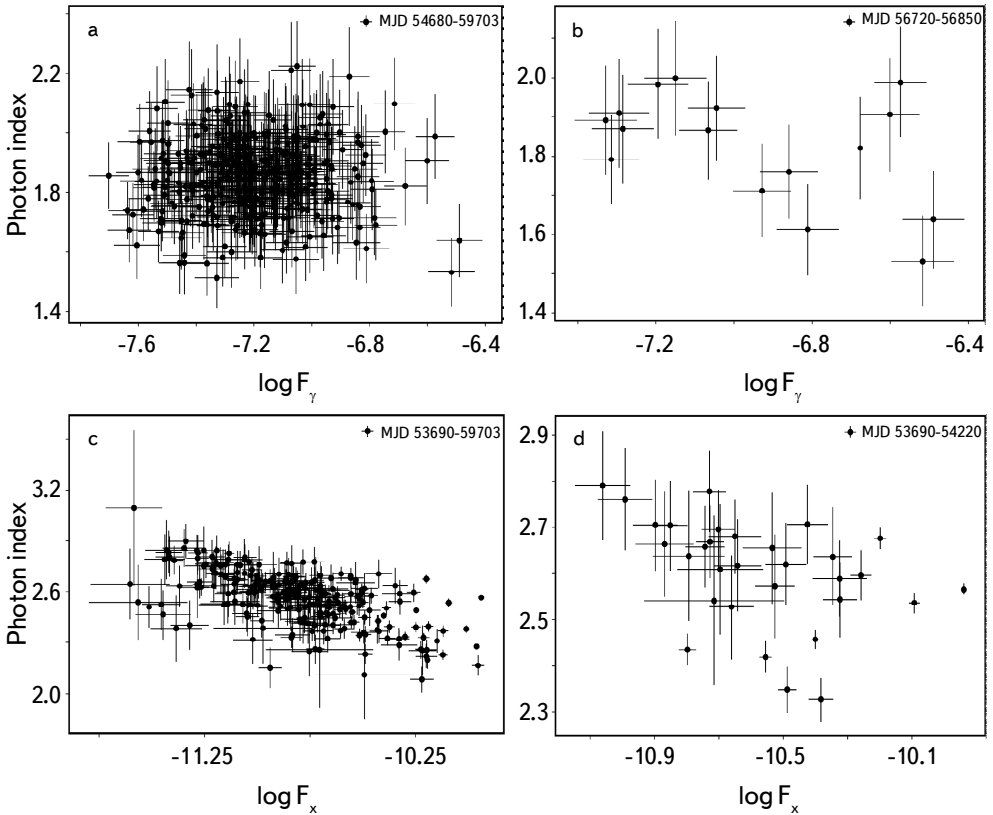


Fig.3. PKS 2155-304  $\gamma$ -ray flux versus photon index variation during the whole considered period (a) and during the flare between MJD 56720-56850 (b). PKS 2155-304 X-ray flux and photon index variation for all Swift XRT observations (c) and during the flare between MJD 53690-54220 (d).

The blazar S5 0716+71 shows different flaring activities as compared with PKS 2155-304. Although there are large flaring activities in the X-ray band (MJD 58130-58460), no significant correlation between the flux and photon index is observed (Fig.4c, d). There is a hint of harder-when-brighter trend during the

X-ray flaring period (Fig.4d) but the linear-Pearson correlation test yields  $r_p = -0.22$  and  $p = 0.13$ . Instead, in the  $\gamma$ -ray band, for the entire and flaring periods,  $r_p = 0.25$  and  $p < 10^{-5}$  and  $r_p = 0.27$  and  $p = 7.4 \cdot 10^{-5}$ , respectively, which show moderate softer-when-brighter trend. This shows that when the flux increases, the photon index softens. Such photon index variation is not very common for blazars but has been occasionally observed (e.g., [30,52-54]). This shows that the PKS 2155-304 and S5 0716+71 flares observed in the X-ray and  $\gamma$ -ray bands are different by their nature and are caused by different processes.

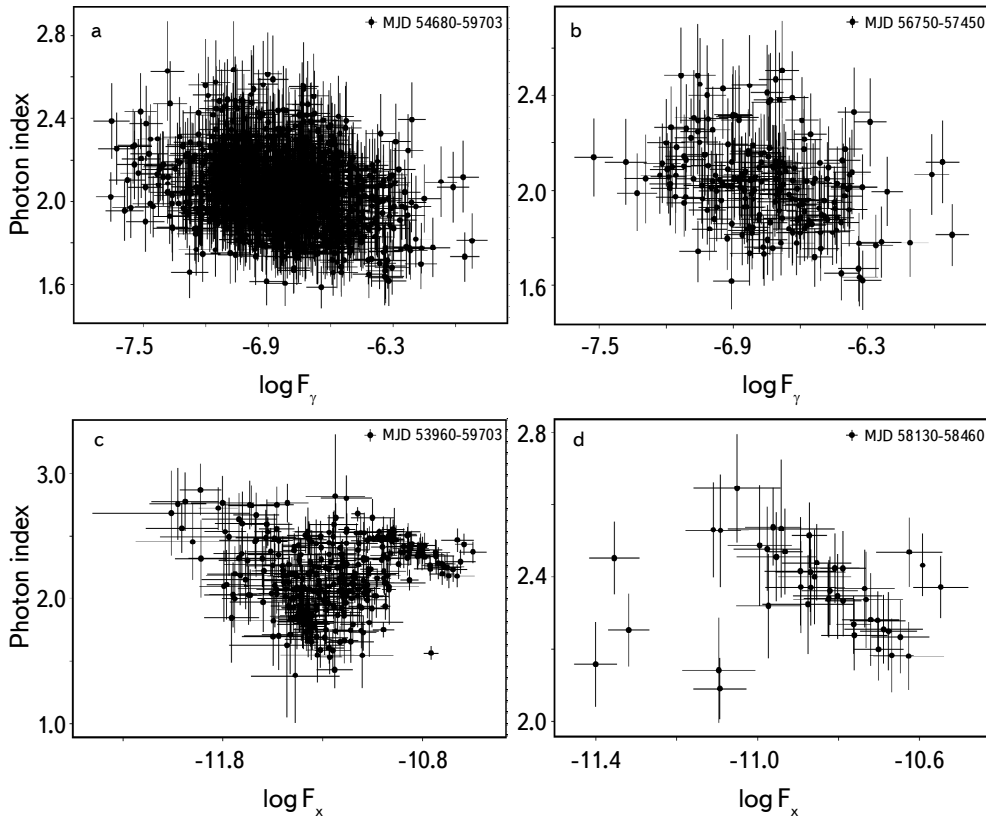


Fig.4. The variation of S5 0716+71  $\gamma$ -ray flux versus photon index for the entire period (a) and flaring period during MJD 56750-57450 (b). Swift XRT measured photon index flux variation for all Swift XRT observations (c) and during the flare between MJD 58130-58460 (d).

**5.2. Correlation studies.** As the multiwavelength light curves in Fig.1 and 2 shows, there seem to be contemporaneous changes in the flux in different bands. In order to test whether or not the emission in different bands are varying contemporaneously, i.e., whether the emission in different bands are related, a Spearman correlation test was applied. The possible correlation was investigated

Table 1

RESULTS OF THE CORRELATION STUDY BETWEEN THE  
EMISSION IN DIFFERENT BANDS

		PKS 2155-304		S5 0716+71	
Band-1	Band-2	Spearman coeff.	$p$ -value	Spearman coeff.	$p$ -value
Optical	X-ray	0.6	1.3e-22	0.7	3e-44
UV	X-ray	0.6	3.5e-30	0.7	1.3e-46
Optical	$\gamma$ -ray	0.7	5.4e-18	0.6	4.8e-18
UV	$\gamma$ -ray	0.8	3.6e-19	0.7	1.3e-18
X-ray	$\gamma$ -ray	0.5	6.1e-8	0.5	2.4e-12

by computing the correlation rank between the emission in different bands, i.e., computing Spearman correlation coefficient  $\rho$ . In order to perform an as general as possible test, the correlation between the emission in the X-ray and  $\gamma$ -ray bands, X-ray and optical/UV bands,  $\gamma$ -ray and optical/UV bands was investigated. When comparing the  $\gamma$ -ray flux with the other bands, the  $\gamma$ -ray periods computed by the adaptive binning method can contain several Swift observations. In this case, the mean of all observations is considered, but a check that the mean value does not significantly differ from the individual estimates in that bin was performed.

The results from the Spearman correlation analysis are given in Table 1 for each two bands providing the coefficient and probability. The results reported in Table 1 show that the null hypothesis that there is no correlation can be rejected in all cases. However, there is no strong correlation between the emissions in different bands. The correlation between the X-ray and  $\gamma$ -ray fluxes of PKS 2155-304 is shown in Fig.5a. There is a weak correlation in these two bands with  $\rho = 0.5$ . For example, when the highest X-ray flux of  $(2.29 \pm 0.1) \cdot 10^{-10}$  erg cm $^{-2}$  s $^{-1}$  was observed, the source was bright in the  $\gamma$ -ray band with a flux of  $(1.43 \pm 0.27) \cdot 10^{-7}$  photon cm $^{-2}$  s $^{-1}$ . For PKS 2155-304, the strongest correlation is found for UV and  $\gamma$ -ray bands,  $\rho = 0.8$  (Fig.5b). There is also a milder correlation between the source emission in X-ray and optical bands with  $\rho = 0.6$  (Fig.5c).

For S5 0716+71, there is again a weak correlation between the emission in the X-ray and  $\gamma$ -ray bands with  $\rho = 0.5$  (Fig.5d). This is because the emission in the X-ray band corresponds to the highest tail of the synchrotron emission, while the emission in the  $\gamma$ -ray band corresponds to the peak of the inverse Compton component. Since the emission comes from electrons of different energy, it is natural to expect a time lag between the emission in these two bands. For this source, the correlation is almost at the same level for the optical/UV vs X-ray and optical/UV vs  $\gamma$ -ray bands (Fig.5e and f).

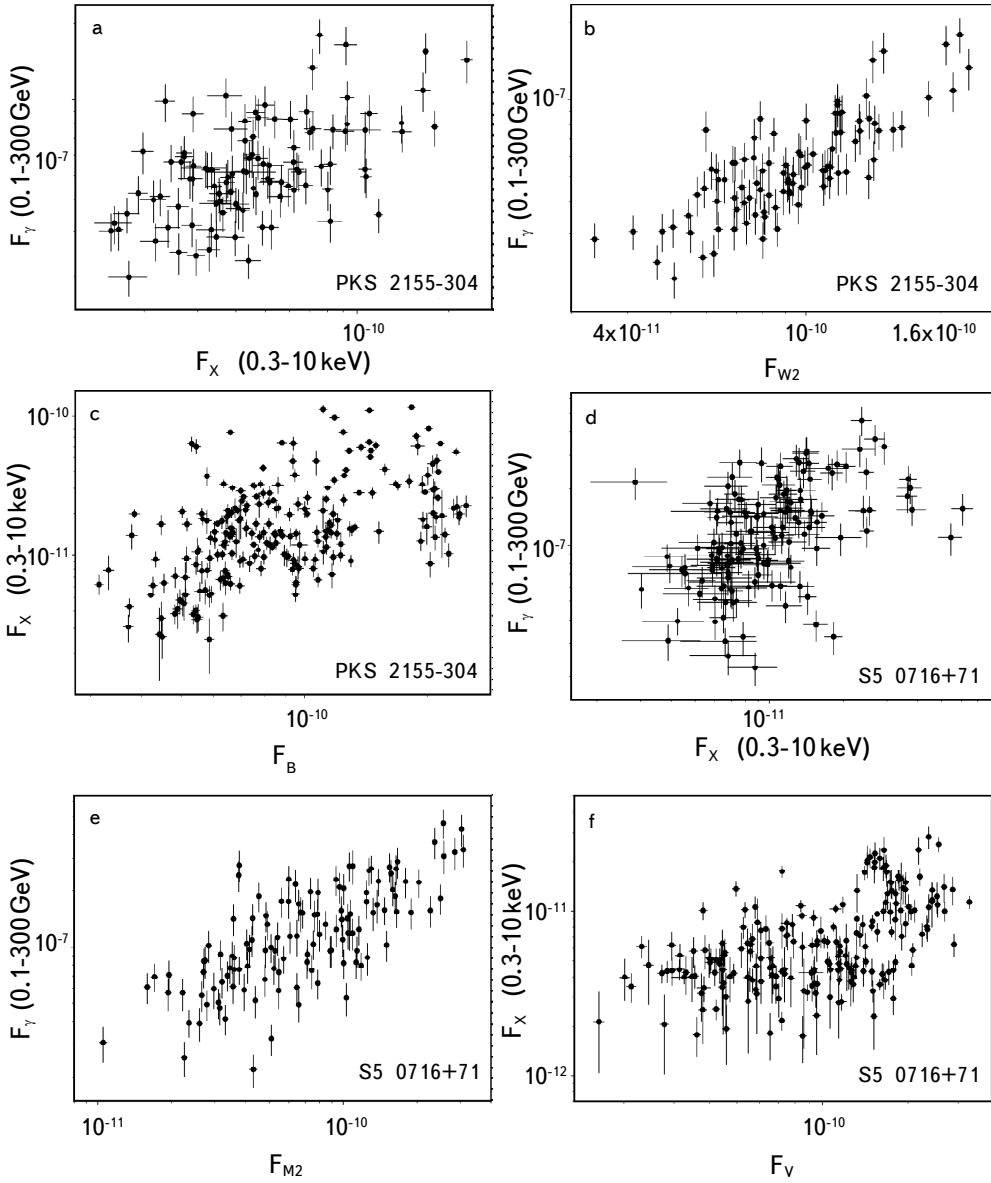


Fig.5. The scatter plot of the flux in different bands.

5.3. *Multiwavelength SEDs.* The available data allows to investigate the broadband spectrum of both sources from radio to VHE  $\gamma$ -ray bands. The variability observed in different bands allows to build the SEDs in different periods and thus to investigate the variability in the energy domain as well. The archival

data for both sources were downloaded from SSDC science data archive<sup>2</sup> and are plotted together with the data analyzed in this paper (optical/UV, X-ray and  $\gamma$ -ray bands).

The multiwavelength SED of PKS 2155-304 is shown in Fig.6a. The archival data are shown in gray and the optical/UV, X-ray and  $\gamma$ -ray data observed during the multiwavelength flare of the source during MJD 56714 - 56903 are in black color. On the average state the peak of the synchrotron component is at  $\sim 10^{16}$  Hz which does not change during the optical/UV flare of the source. It is interesting that the optical/UV flux has increased by a factor of nearly 10, but the peak of the synchrotron component is unchanged. The variability in the X-ray band is even at higher amplitudes, and the historical X-ray flux changes by a factor of 100. The same high amplitude variability can be seen also in the HE  $\gamma$ -ray band. When comparing the flux in the HE and VHE  $\gamma$ -ray bands it is necessary to take into account the strong absorption of GeV/TeV photons through interaction with extragalactic background light (EBL) photons. This means that the rising shape in the MeV/GeV band, which implies that the peak of the inverse Compton component is around  $\sim 10^{26}$ - $10^{27}$  Hz, will exponentially decrease at higher energies, being in agreement with the observed GeV/TeV data.

In the optical/UV band, the variability of S5 0716+71 (Fig.6b) is even more extreme when the lowest and highest fluxes differ almost by a factor of 100. In this case, the optical/UV data with a decreasing shape are defining the decay of the synchrotron component, while for PKS 2155-304 these data correspond to the rising part of the synchrotron component. For S5 0716+71, also a high-amplitude variability is observed in the X-ray and  $\gamma$ -ray bands. Given the large

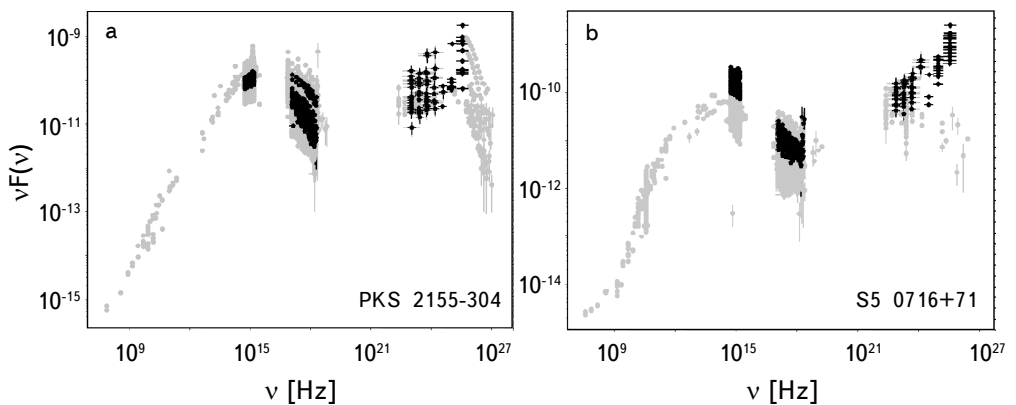


Fig.6. The multiwavelength SEDs of PKS 2155-304 (a) and S5 0716+71 (b) during the considered period.

<sup>2</sup> <https://www.ssdsc.asi.it>

red shift of S5 0716+71, the EBL absorption is even stronger for this source, which can explain the large difference between the Fermi spectrum (although not contemporaneous) and MAGIC measurements (three VHE  $\gamma$ -ray points).

The SEDs of PKS 2155-304 and S5 0716+71 can be modeled by synchrotron/synchrotron self-Compton (SSC) model [55,56]. In this scenario, the energetic electrons confined in a compact emitting region in a randomly oriented magnetic field emit via synchrotron radiation which explains the first peak in the SED while the second peak is due to inverse Compton scattering of the same synchrotron photons. The observed flux increase in the optical/UV bands can be either due to variations in the injected plasma (particles) or due to the change of the magnetic field, as the synchrotron luminosity depends on the product of  $N_e$  (distribution of electrons) and  $B^2$ . If there is an injection of new electrons in the emitting region (e.g., due to re-acceleration) or the magnetic field increases in the emitting region (e.g., due to the change of particle density), the synchrotron luminosity will increase, appearing as a flare in the radio-optical/UV-X-ray bands. Moreover, in this interpretation the available X-ray data can be used to limit the maximum energy of accelerated particles.

The difference in the variability in the optical/UV and X-ray bands can be naturally explained by a simple consideration of particle acceleration and cooling. The X-ray emission is produced from the highest energy electrons which have shorter cooling time (the electron cooling time is inverse proportional to the electron energy,  $t_{cool} \sim 1/E_e$ ), while in the same magnetic field the optical/UV emission is from electrons that have lower energy and thus a longer cooling time. So, when there are new electrons injected in the emitting region, the emission in the X-ray band will vary with an amplitude higher than is seen in Fig.6.

**6. Summary.** The results of the PKS 2155-304 and S5 0716+71 observations in the UV/optical, X-ray and  $\gamma$ -ray bands are reported. The multiwavelength monitoring of blazars is a unique tool to infer the physical processes dominating in the relativistic jets. These two blazars show prominent flares in the optical/UV bands, but it is shown that the flux substantially varies also in other bands. With the increase of the X-ray flux of PKS 2155-304, the photon index hardens, showing a harder-when-brighter trend. Instead, a moderate softer-when-brighter trend is observed in the  $\gamma$ -ray band for S5 0716+71. Generally, both sources show high-amplitude flares in the  $\gamma$ -ray band; the maximum  $\gamma$ -ray luminosity of PKS 2155-304 is  $L_\gamma = 1.35 \cdot 10^{47}$  erg s<sup>-1</sup> while it is  $L_\gamma = 2.13 \cdot 10^{48}$  erg s<sup>-1</sup> for S5 0716+71.

The correlation analysis shows that there is a strong correlation for PKS 2155-304 emission in the UV and  $\gamma$ -ray bands with Spearman coefficient of  $\rho = 0.8$ . This suggests a common origin of the emission in these bands, i.e., the emission

in these bands is produced by the same electrons. In particular, most likely the UV emission comes from the synchrotron emission from the same electrons that are emitting also in the  $\gamma$ -ray band. This interpretation is even stronger when considering that UV emission defines the rising part of the synchrotron spectrum, as the  $\gamma$ -ray band corresponds to the rising part of the SSC component. In the case of S5 0716+71, as the synchrotron component peaks at lower frequencies, the optical/UV and X-ray bands are defining the high-energy tail of the synchrotron component, so these bands are not correlated with the  $\gamma$ -ray band which again corresponds to the rising part of the SSC component. Instead, as expected, the correlation between the optical/UV and X-ray bands is stronger with  $\rho = 0.8$ .

*Acknowledgements.* I would like to thank N.Sahakyan for helpful discussions and constructive suggestions. This work was supported by the Science Committee of RA, in the frames of the research project No 20TTCG-1C015. This work was made possible in part by a research grant from the Yervant Terzian Armenian National Science and Education Fund (ANSEF) based in New York, USA.

ICRANet Armenia Marshall Baghramian Avenue 24a, 0019 Yerevan,  
Armenia, e-mail: davidisrayelyan@gmail.com

## МНОГОВОЛНОВЫЕ НАБЛЮДЕНИЯ БЛАЗАРОВ PKS 2155-304 И S5 0716+71

Д.ИСРАЕЛЯН

Изучение многоволновых эмиссионных свойств блазарных струй позволяет пролить свет на механизмы ускорения частиц и эмиссии, происходящие в них. Излучение ярких блазаров PKS 2155-304 ( $z=0.116$ ) и S5 0716+71 ( $z=0.31$ ) в оптическом/УФ, рентгеновском и  $\gamma$ -диапазонах исследовано путем анализа данных телескопов Fermi-LAT, Swift XRT и Swift UVOT. Многоволновые кривые блеска обоих источников в этих диапазонах показывают множественные пики при значительном увеличении потока. В оптическом/УФ-диапазонах поток обоих источников возрастал выше  $2 \cdot 10^{-10}$  эрг см<sup>-2</sup> с<sup>-1</sup>. Рентгеновское излучение PKS 2155-304 характеризовалось тенденцией "жестче, когда ярче", тогда как  $\gamma$ -излучение S5 0716+71 показало умеренную тенденцию "мягче, когда ярче". Корреляционный анализ показывает сильную корреляцию между УФ- и  $\gamma$ -излучением PKS 2155-304, в то время как существует корреляция

между оптическим/УФ- и рентгеновским излучением S5 0716+71. Наблюдаемое широкополосное спектральное распределение энергии обоих источников, а также наблюдаемая изменчивость и корреляции могут быть объяснены в рамках моделей однозонного синхротрона/синхротрона-самокомптона.

Ключевые слова: *PKS 2155-304: S5 0716+71: гамма излучение: рентгеновское излучение: блазары*

## REFERENCES

1. C.M.Urry, P.Padovani, Publ. Astron. Soc. Pacif., **107**, 803, 1995.
2. A.Abdo, M.Ackermann, M.Ajello et al., Astrophys. J., **710**, 810, 2010.
3. J.R.P.Angel, H.S.Stockman, Ann. Rev. Astron., **18**, 321, 1980.
4. A.R.G.Mead, K.R.Ballard et al., Astron. Astrophys., **83**, 183, 1990.
5. C.D.Derner, R.Schlickeiser, A.Mastichiadis, Astron. Astrophys., **256**, L27, 1992.
6. M.Sikora, M.Begelman, M.Rees, Astrophys. J., **421**, 153, 1994.
7. A.Mucke, R.Protheroe, Astroparticle Physics, **15**, 121, 2001.
8. K.Mannheim, Astron. Astrophys., **269**, 67, 1993.
9. K.Mannheim, P.L.Biermann, Astron. Astrophys., **221**, 211, 1989.
10. A.Mucke, R.Protheroe, R.Engel et al., Astroparticle Physics, **18**, 593, 2003.
11. M.Böttcher, A.Reimer, K.Sweeney et al., Astrophys. J., **54**, 768, 2013.
12. S.Ansoldi, L.A.Antonelli, C.Arcaro et al., Astrophys. J., **863**, L10, 2018.
13. A.Keivani, K.Murase, M.Petropoulou et al., Astrophys. J., **864**, 16, 2018.
14. K.Murase, F.Oikonomou, M.Petropoulou, Astrophys. J., **865**, 124, 2018.
15. P.Padovani, P.Giommi, E.Resconi et al., Mon. Not. Roy. Astron. Soc., **480**, 192, 2018.
16. N.Sahakyan, Astrophys. J., **866**, 109, 2018.
17. C.Righi, F.Tavecchio, L.Pacciani, Mon. Not. Roy. Astron. Soc., **484**, 2067, 2019.
18. M.Cerruti, A.Zech, C.Boisson, Mon. Not. Roy. Astron. Soc., **483**, L12, 2019.
19. N.Sahakyan, Astron. Astrophys., **622**, A144, 2019.
20. S.Gao, A.Fedynitch, W.Winter et al., Nat. Astron., **3**, 88, 2019.
21. S.Gasparyan, D.Begue, N.Sahakyan, Mon. Not. Roy. Astron. Soc., **509**, 2102, 2022.
22. MAGIC Collaboration, Astron. Astrophys., **623**, A175, 2019.
23. M.Ackermann, Astrophys. J., **824**, L20, 2016.
24. T.Hovatta, M.Tornikoski, M.Lainela et al., Astron. Astrophys., **469**, 899, 2007.
25. M.Villata, C.M.Raiteri, H.D.Aller et al., Astron. Astrophys., **424**, 497, 2004.
26. N.Gehrels, G.Chinacarini, P.Giommi et al., Astrophys. J., **611**, 1005, 2004.
27. P.W.A.Roming, T.E.Kennedy, K.O.Mason et al., Space Sci. Rev., **120**, 95, 2005.
28. D.N.Burrows, J.E.Hill, J.A.Nousek et al., Space Sci. Rev., **120**, 165, 2005.

29. *S.D.Barthelmy, L.M.Barbier, J.R.Cummings et al.*, Space Sci. Rev., **120**, 143, 2005.
30. *P.Giommi, M.Perri, M.Capalbi et al.*, Mon. Not. Roy. Astron. Soc., **507**, 5690, 2021.
31. *T.Poole, A.Breeveld, M.Page et al.*, Mon. Not. Roy. Astron. Soc., **383**, 627, 2008.
32. *W.Cash*, Astrophys. J., **228**, 939, 1979.
33. HI4PI Collaboration, Astron. Astrophys., **594**, A116, 2016.
34. *P.M.W.Kalberla, W.B.Burton, D.Hartman et al.*, Astron. Astrophys., **440**, 775, 2005.
35. *J.M.Dickey, F.J.Lockman*, Ann. Rev. Astron., **28**, 215, 1990.
36. *W.B.Atwood, A.A.Abdo, M.Ackermann et al.*, Astrophys. J., **697**, 1071, 2009.
37. *M.Ajello, R.Angioni, M.Axelsson et al.*, Astrophys. J., **892**, 105, 2020.
38. *S.Gasparyan, N.Sahakyan, V.Baghmanyanyan et al.*, Astrophys. J., **863**, 114, 2018.
39. *N.Sahakyan, V.Baghmanyanyan, D.Zargaryan*, Astron. Astrophys., **614**, A6, 2018.
40. *D.Zargaryan, S.Gasparyan, V.Baghmanyanyan et al.*, Astron. Astrophys., **608**, A37, 2017.
41. *V.Baghmanyanyan, S.Gasparyan, N.Sahakyan*, Astrophys. J., **848**, 111, 2017.
42. *R.J.Britto, E.Bottacini, B.Lott et al.*, Astrophys. J., **830**, 162, 2016.
43. *B.Rani, T.P.Krichbaun, L.Fuhrmann et al.*, Astron. Astrophys., **552**, A11, 2013.
44. *A.J.Shimmings, J.G.Bolton*, AuJPA, **32**, 1, 1974.
45. *D.A.Schwartz, R.E.Doxsey, R.E.Griffiths et al.*, Astrophys. J. Lett., **229**, L53, 1979.
46. *W.T.Vestrand*, Astrophys. J. Lett., **454**, L93, 1995.
47. *O.Chadwick, L.Derry, P.Vitousek et al.*, Nature, **397**, 491, 1999.
48. *K.Nilsson, T.Pursimo, A.Sillanpää et al.*, Astron. Astrophys., **487**, L29, 2008.
49. *V.S.Bychkova, A.E.Vol'vach, N.S.Kardashev et al.*, Astron. Rep., **59**, 851, 2015.
50. MAGIC Collaboration, Astron. Astrophys., **619**, A45, 2018.
51. *J.G.Kirk, F.M.Rieger, A.Mastichiadis*, Astron. Astrophys., **333**, 452, 1998.
52. *N.Sahakyan, P.Giommi*, Mon. Not. Roy. Astron. Soc., **513**, 4645, 2022.
53. *B.Kapanadze, S.Vercellone, P.Romano et al.*, Mon. Not. Roy. Astron. Soc., **480**, 407, 2018.
54. *S.Komossa, D.Grupe, M.L.Parker et al.*, Mon. Not. Roy. Astron. Soc., **504**, 5575, 2021.
55. *S.D.Bloom, A.P.Marscher*, Astrophys. J., **461**, 657, 1996.
56. *G.Ghisellini, L.Maraschi, A.Treves*, Astron. Astrophys., **146**, 204, 1985.